High-spin Mn–oxo complexes and their relevance to the oxygen-evolving complex within photosystem II

Rupal Gupta[a], Taketo Taguchi[b], Benedikt Lassalle-Kaiser[c], Emile L. Bominaar[a], Junko Yano[c], Michael P. Hendrich[a], and A. S. Borovik[b,1]

[a]Department of Chemistry, Carnegie Mellon University, Pittsburgh, PA 15213; [b]Department of Chemistry, University of California, Irvine, CA 92697; and [c]Physical Biosciences Division, Lawrence Berkeley National Laboratory, Berkeley, CA 94720

Edited by Harry B. Gray, California Institute of Technology, Pasadena, CA, and approved February 18, 2015 (received for review November 29, 2014)

The structural and electronic properties of a series of manganese complexes with terminal oxido ligands are described. The complexes span three different oxidation states at the manganese center (III–V), have similar molecular structures, and contain intramolecular hydrogen-bonding networks surrounding the Mn–oxo unit. Structural studies using X-ray absorption methods indicated that each complex is mononuclear and that oxidation occurs at the manganese centers, which is also supported by electron paramagnetic resonance (EPR) studies. This gives a high-spin Mn^{V}–oxo complex and not a Mn^{IV}–oxy radical as the most oxidized species. In addition, the EPR findings demonstrated that the Fermi contact term could experimentally substantiate the oxidation states at the manganese centers and the covalency in the metal–ligand bonding. Oxygen-17–labeled samples were used to determine spin density within the Mn–oxo unit, with the greatest delocalization occurring within the Mn^{V}–oxo species (0.45 spins on the oxido ligand). The experimental results coupled with density functional theory studies show a large amount of covalency within the Mn–oxo bonds. Finally, these results are examined within the context of possible mechanisms associated with photosynthetic water oxidation; specifically, the possible identity of the proposed high valent Mn–oxo species that is postulated to form during turnover is discussed.

metal–oxo complexes | water oxidation | inorganic chemistry | photosynthesis | oxygen-evolving complex

Photosynthetic water oxidation is an essential chemical reaction that is responsible for producing Earth's aerobic environment. Dioxygen production occurs at the active site of the enzyme photosystem II, referred to as the oxygen-evolving complex (OEC), which contains a unique Mn_4CaO cluster (1, 2). Several features of the OEC are known, including an approximate arrangement of the metal ions within the cluster (Fig. 1*A*) (3, 4), its structural flexibility during turnover (5, 6), and its ability to store oxidizing equivalents via five photo-induced redox states (S_i, i = 0–4 and known as the Kok cycle) (7). Substrate water molecules bind to the cluster and, upon oxidation, are coupled to produce dioxygen and 4 eq of protons. There is agreement that formation of the O–O bond occurs in the highest oxidized state of the Mn_4CaO_5 cluster (S_4), after which the cluster reverts to the most reduced state, S_0 (1–6, 8–10). The transient S_4 state has eluded detection, making it difficult to experimentally probe the structural and physical requirements necessary to promote dioxygen production. Magnetic resonance and density functional theory (DFT) studies of the S_2 and S_3 states have been used to infer that the beginning and ending oxidation states of the Kok cycle are $Mn_3^{III}Mn^{IV}$ (S_0) and $Mn_3^{IV}Mn^{V}$ or $Mn_3^{IV}Mn^{IV}$ O• (S_4) (11–14). The location of the Mn^{V} center within the cluster is not certain, yet one possibility is the dangling Mn_{A4} site, which is coordinated to anionic donors and is surrounded by a network of hydrogen bonds (H bonds) (8–10).

The lack of experimental information about the transient S_4 state has further prevented a consensus opinion on how initial O–O bond formation occurs. Quantum chemical studies have provided insight into this process with two limiting mechanisms (11–14). In one mechanism, a Ca^{II}–OH (or –OH_2) unit serves as a nucleophile and attacks an electrophilic Mn–oxo center within the cluster (8–10, 14, 15). The dangling Mn_{A4}–oxo center (Fig. 1*B*) or the μ_3-oxo ligand (O5) that bridges between two of the Mn centers and the Ca^{II} ion are possible electrophilic centers for attack. In a second mechanism, a radical process is proposed in which an oxyl radical coupling occurs between O5 and some other oxido ligand that is bonded to the cluster, possibly at Mn_{D1} (Fig. 1*C*) (11, 12). Central to both of these mechanisms is that forming an O–O bond involves a high valent Mn center with a terminal oxido ligand (Mn–oxo), which most computational reports suggest is a Mn^{IV}–oxyl radical (Mn^{IV}–O•) rather than the isoelectronic Mn^{V}–oxo species (11–14). However, there is currently no experimental precedent for an oxyl species in a complex containing a first-row transition metal ion.

An alternative approach to exploring possible intermediates in O–O bond formation is to develop synthetic systems with Mn–oxo species and investigate spectroscopically whether they support either a Mn^{V}–oxo state or a Mn^{IV}–oxyl state (16–18). We have thus prepared a series of monomeric Mn–oxo complexes $[Mn^{n}H_3buea(O)]^{m}$ (n = 3+ to 5+; m = 2− to 0) in which $[H_3buea]^{3-}$ provides a strong anionic ligand field while maintaining local C_3 symmetry around the manganese centers (Fig. 1*D*) (19–21). The $[H_3buea]^{3-}$ ligand also controls the local environment surrounding the Mn–oxo unit via intramolecular H bonds. These structural components produce Mn–oxo complexes that are approximate models for the manganese centers within the OEC, especially Mn_{A4}, which is also coordinated to anionic donors and is surrounded by a network of H bonds. The local C_3 symmetry of the $[Mn^{n}H_3buea(O)]^{m}$ complexes affords high-spin

Significance

Metal complexes with terminal oxido ligands are important in a wide variety of transformations, including a high valent manganese-oxido unit that is involved in the O–O bond-forming step in photosynthetic water oxidation. Theoretical proposals suggest that a Mn^{IV}–oxyl radical species is present, yet such species have not been observed experimentally. Using a combination of experimental measurements and theoretical calculations, we show here that the bonding within the Mn–oxido unit is best described as highly covalent, with 0.45 spins on the oxido ligand. These findings offer a counter explanation for the putative high valent manganese species in photosynthesis as an energetically accessible, high-spin Mn^{V}–oxido unit instead of a Mn^{IV}–oxyl radical species.

Author contributions: R.G., T.T., E.L.B., J.Y., M.P.H., and A.S.B. designed research; R.G., T.T., B.L.-K., E.L.B., and M.P.H. performed research; R.G., T.T., B.L.-K., J.Y., M.P.H., and A.S.B. analyzed data; and J.Y., M.P.H., and A.S.B. wrote the paper.

The authors declare no conflict of interest.

This article is a PNAS Direct Submission.

See Commentary on page 5265.

[1]To whom correspondence should be addressed. Email: aborovik@uci.edu.

This article contains supporting information online at www.pnas.org/lookup/suppl/doi:10.1073/pnas.1422800112/-/DCSupplemental.

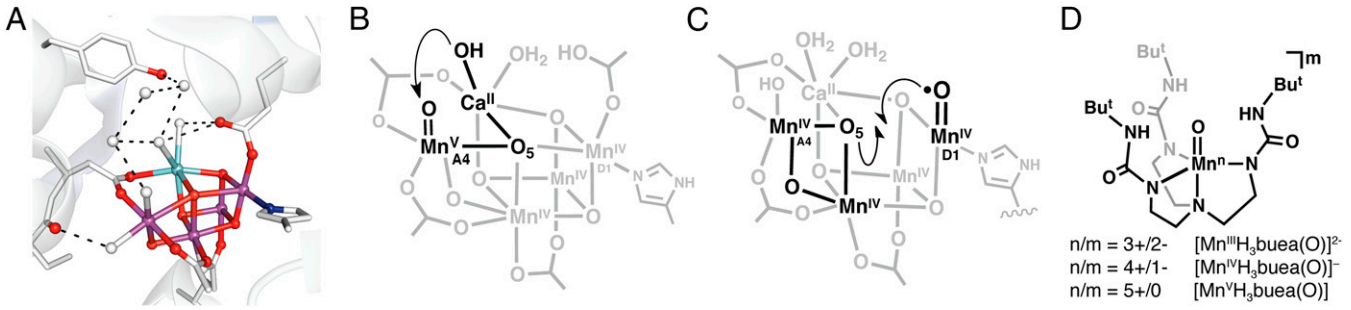

Fig. 1. (*A–D*) Structures of the OEC cluster illustrating the hydrogen-bonding network (*A*) (purple spheres, Mn; light blue spheres, Ca^{2+}; red spheres, oxido/hydroxo ligands; blue sphere, nitrogen; white spheres, water), the nucleophilic mechanism for O–O bond formation (*B*), the radical coupling mechanism for O–O bond formation (*C*), and the Mn–oxo complexes used in this study (*D*). The structure in *A* is adapted from Protein Data Bank ID 3BZ1.

species that can be characterized with electron paramagnetic resonance (EPR) spectroscopy. The spectra provide an experimental probe of the electron distribution within the Mn–oxo unit and the spin density on the oxido ligand. Moreover, this series provided the first opportunity to examine the correlation between covalency within the Mn–O bond, the experimental Fermi contact hyperfine constant for ^{55}Mn, and spin densities. Our findings establish that there is unpaired spin density on the oxido ligand in $[Mn^{V}H_3buea(O)]$, yet the density is less than what is expected for an oxyl radical; this offers the possibility that a high-spin Mn^{V}–oxo center could be operative within S_4 of the OEC.

Results

Structural Properties. X-ray absorption spectroscopy (XAS) was used to investigate the structural properties of the three $[Mn^{n}H_3buea(O)]^{m}$ complexes. X-ray near-edge absorption spectra (XANES) collected on the Mn–oxo complexes showed edge shifts that were consistent with sequential oxidation of the manganese centers (Fig. S1 and Table S1). An edge energy shift of ∼2.5 eV, measured at the half-edge jump, was observed for the one-electron oxidation from $[Mn^{III}H_3buea(O)]^{2-}$ (65549.2 eV) to $[Mn^{IV}H_3buea(O)]^{-}$ (6551.72 eV). A similar energy shift of ∼3.3 eV was observed in the XANES for the related Mn–OH complexes $[Mn^{III}H_3buea(OH)]^{-}$ and $[Mn^{IV}H_3buea(OH)]$ (22). The energy is further shifted upon oxidation of $[Mn^{IV}H_3buea(O)]^{-}$ to $[Mn^{V}H_3buea(O)]$ (6553.02 eV), although by a smaller amount (∼1.3 eV). [A small amount of $[Mn^{IV}H_3buea(O)]^{-}$ (∼10%) was present in the sample that was determined by EPR spectroscopy—this amount was subtracted from the spectrum prior to analysis.] In addition, a significant increase in the intensity of the preedge peak was observed upon oxidation to $[Mn^{V}H_3buea(O)]$, which reflects the shortening of the Mn–O bond length compared with that of the other $[Mn^{n}H_3buea(O)]^{m}$ complexes (Fig. S2); the intensity of this peak is correlated to the extent of Mn 3d-4p mixing, which increases with decreasing Mn–O bond distance. However, the preedge intensity of $[Mn^{V}H_3buea(O)]$ is not as strong as the peaks found for square pyramidal low-spin Mn^{V}–oxo complexes, which have short Mn–O bond lengths of less than 1.6 Å (Fig. S3 and Table S1) (similar increases in the preedge features have been reported for other Mn^{V}–oxo complexes) (23, 24). The preedge intensity has been shown (24) to strongly depend on the ligand symmetry and Mn-ligand distances, and a longer Mn^{V}–O bond distance will decrease the degree of Mn-3d-4p mixing. The observed intensity of the preedge peak in $[Mn^{V}H_3buea(O)]$ suggests that its Mn–O bond distance should be relatively long for a Mn^{V}–oxo complex, which is supported by extended X-ray absorption fine structure (EXAFS) results (see below). A weak preedge intensity of $[Mn^{V}H_3buea(O)]$ has also been predicted by Leto and Jackson (25) from a TD-DFT calculation, in which they described the detailed relationships between Mn–O bond lengths, coordination geometries, and the preedge intensities.

Results from EXAFS spectra on the Mn–oxo complexes further support the sequential oxidation of $[Mn^{III}H_3buea(O)]^{2-}$ (Figs. S4 and S5). The molecular structure of $[Mn^{III}H_3buea(O)]^{2-}$ has already been characterized using X-ray diffraction (XRD) methods (19), and the structural results obtained by EXAFS curve fitting are in agreement with the XRD-determined structure. From XRD methods, $[Mn^{III}H_3buea(O)]^{2-}$ was found to contain a trigonal bipyramidal coordination geometry around the manganese center in which the oxido ligand is bonded *trans* to the apical nitrogen donor to form an N_4O primary coordination sphere. EXAFS analysis for $[Mn^{III}H_3buea(O)]^{2-}$ found one Mn–O bond length of 1.78(2) Å and four Mn–N bond distances of 2.07(2) Å that are nearly the same as those found by XRD (Table 1 and Table S2). The EXAFS data for $[Mn^{IV}H_3buea(O)]^{-}$ gave an Mn–O bond distance of 1.76(3) Å, which is statistically the same as that found in $[Mn^{III}H_3buea(O)]^{2-}$. The EXAFS analyses were best fitted to four Mn–N bonds at a distance of 2.00(2) Å, which is a contraction of 0.07 Å from those found in $[Mn^{III}H_3buea(O)]^{2-}$. Similar trends in Mn–O and Mn–N bond lengths were found for $[Mn^{III}H_3buea(OH)]^{-}$ and $[Mn^{IV}H_3buea(OH)]^{-}$; that is, the Mn–O bond distances are similar in the Mn^{III}–OH and Mn^{IV}–OH complexes, but the Mn–N bond lengths are significantly shorter in $[Mn^{IV}H_3buea(OH)]$ (22). The N_4O primary coordination sphere around the manganese center was maintained in $[Mn^{V}H_3buea(O)]$, with further oxidation causing significant shortening of the Mn–X bond lengths (Table 1). The best fit of the EXAFS data gave one Mn–O bond distance of 1.68(4) Å and four Mn–N bond distances of 1.86(5) Å for $[Mn^{V}H_3buea(O)]$, which represent a contraction in bond distances of ∼0.1 for the Mn–O bond and 0.14 Å for the Mn–N bonds compared with $[Mn^{IV}H_3buea(O)]^{-}$.

DFT Analysis. The geometry-optimized structures obtained from spin-unrestricted density functional theory (DFT) calculations showed that each $[Mn^{n}H_3buea(O)]^{m}$ complex adopted a monomeric five-coordinated structure with metrical parameters that agreed

Table 1. Structural and EXAFS fitting parameters for the $[Mn^{n}H_3buea(O)]^{m}$ complexes

			R, Å		
n	Shell	No.	DFT	XRD	EXAFS
III	Mn–O	1	1.767	1.771 (5)	1.78 (2)
	Mn–N*	4	2.12	2.100 (5)	2.07 (2)
IV	Mn–O	1	1.705	—	1.76 (3)
	Mn–N*	4	2.12	—	2.00 (2)
V	Mn–O	1	1.679	—	1.68 (4)
	Mn–N*	4	1.95	—	1.86 (5)

Values in parentheses are the errors associated with the measurement.
*Average value.

with those obtained from our experimental measurements (Table 1) (20). For $[Mn^{III}H_3buea(O)]^{2-}$, the Mn–O bond length of 1.767 Å from DFT calculations matched those obtained from XRD [1.771(5) Å] and EXAFS [1.78(2) Å]. Similar good agreement between calculations and experiment was found for the average Mn–N bond length (Table 1). Upon oxidation to $[Mn^{IV}H_3buea(O)]^{-}$, the DFT calculations predicted that the Mn–O bond contracts to 1.705 Å, a somewhat larger change than was found by EXAFS experiments (Table 1). Similarly, the average Mn–N bond length differs by nearly 0.05 Å. A strong match was found between theory and experiment for the molecular structure of $[Mn^{V}H_3buea(O)]$: the Mn–O and average Mn–N bond distances of 1.679 and 1.86 Å obtained from DFT calculations were identical to those determined from EXAFS measurements. The DFT calculations also found that all $[Mn^{n}H_3buea(O)]^{m}$ complexes are high spin as anticipated for Mn–oxo complexes with local trigonal symmetry, which requires that the orbitals {xz, yz} and {x^2-y^2, xy} form degenerate pairs that transform as *E* representations. The calculations predict that the three trigonal angles (N_{urea}–Mn–$N_{urea'}$) are equal in $[Mn^{III}H_3buea(O)]^{2-}$ and $[Mn^{V}H_3buea(O)]$, whereas in $[Mn^{IV}H_3buea(O)]^{-}$, single occupation of one of these *E* levels causes a Jahn–Teller distortion that leads to different values for the three N_{urea}–Mn–$N_{urea'}$ angles (Table S3). Our computational results also agree with those reported recently using time-dependent density functional theory (TD-DFT) methods (25). Our results also show that the Mn–oxo bonds in the series of $[Mn^{n}H_3buea(O)]^{m}$ complexes are best described as having a formal bond order of 2, in which an empty z^2 orbital and two half-filled xz and yz orbitals are involved in the bonding.

EPR Spectroscopy: $[Mn^{III}H_3buea(O)]^{2-}$. We have previously reported EPR results (21) for the oxidative titration of $[Mn^{III}H_3buea(O)]^{2-}$ and here we extend this previous work to include ^{55}Mn and ^{17}O hyperfine measurements as well as DFT calculations to provide more detailed descriptions of the bonding in the $[Mn^{n}H_3buea(O)]^{m}$ complexes. The S = 2 ground spin state for $[Mn^{III}H_3buea(O)]^{2-}$ was confirmed using X- and Q-band parallel-mode EPR spectroscopy (Fig. 2). The spectra showed a six-line hyperfine splitting of A = 280 MHz (10.0 mT for X-band) at g = 8.08. Simulation of the X-band spectrum predicted the additional broad feature at g = 4.45 from the $|1^{\pm}>$ transition and the g = 8.08 signal from the $|2^{\pm}>$ transition, which are at energies of 2 cm^{-1} and 8 cm^{-1}, respectively, above the ground |0> state of the S = 2 spin manifold. The signals are sensitive only to the z component of **g** and **A** tensors, and because the complex has axial symmetry, this component is aligned with the Mn–O bond. The temperature dependence (Fig. S6) of the signals indicated a zero-field splitting of D = +2.0(2) cm^{-1}, and the simulations predicted the signal shape and intensities for spectra collected at both microwave frequencies using an S = 2 electronic spin, an I = 5/2 nuclear spin, and the parameters found in Table 2. The signal intensity was in quantitative agreement with the sample concentration determined from the weight of the complex added to solvent.

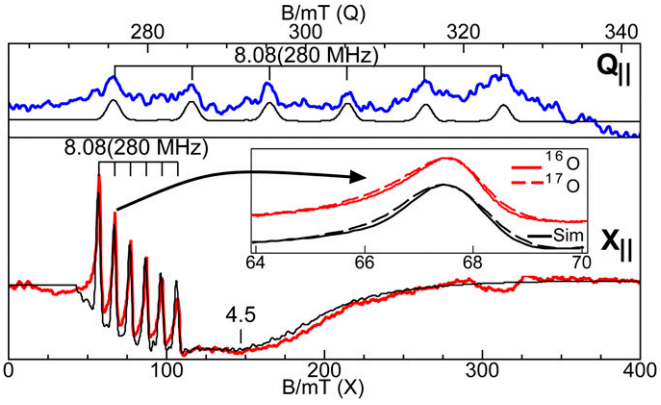

Fig. 2. Q- and X-band parallel-mode EPR spectra of the Mn^{III}–oxo complex, 10 mM in 1:1 dimethyformamide (DMF):tetrahydrofuran (THF). The colored traces are experimental data and the black traces are simulation of the corresponding spectra using the parameters given in Table 2. *Inset* shows the broadening of a hyperfine line at 68 mT due to ^{17}O enrichment. Experimental conditions: temperature 10 K; frequency 33.906 GHz (Q), 9.298 GHz (X); and power 5 mW (Q), 20 mW (X).

$[Mn^{IV}H_3buea(O)]^{-}$. The X- and S-band perpendicular-mode EPR spectra of $[Mn^{IV}H_3buea(O)]^{-}$ gave observed g values that are indicative of an S = 3/2 complex (Fig. 3). The $|\pm3/2>$ excited state doublet is 5.5 cm^{-1} higher in energy than the $|\pm1/2>$ ground state doublet. A large E/D value of 0.264 was found, which is indicative of rhombic symmetry caused by a Jahn–Teller distortion that is expected for a Mn^{IV} center in trigonal symmetry. Overlapping rhombic signals from each doublet result in complicated spectra with only the lower field resonances showing resolved hyperfine patterns. However, the data and simulations from spectra recorded at the two microwave frequencies (Fig. 3) allowed determination of the full ^{55}Mn hyperfine **A** tensor, to give the parameters listed in Table 2. The hyperfine patterns at g = 5.26 ($|\pm1/2>$, A = 189 MHz, or 6.8 mT for X-band) and g = 5.64 ($|\pm3/2>$, A = 222 MHz, or 7.9 mT for X-band) correspond to different directions in the principal axes frame of the **D** tensor. The A values obtained directly from the spectra of $[Mn^{IV}H_3buea(O)]^{-}$ may not be the principal components because the ^{55}Mn **A** tensor may not be collinear with the **D** tensor. Therefore, the simulations (Fig. 3) were generated using the spin-dipolar **A** tensor (+34 MHz, +11 MHz, −45 MHz; S = 3/2) from the DFT optimized structure while varying the isotropic Fermi contact term (A^{FC}) and the rotation angles of **A** relative to **D**. The principal components of the **A** tensor are given in Table 2 and the **A** tensor is rotated relative to the **D** tensor by 36° about the *y* axis.

$[Mn^{V}H_3buea(O)]$. This Mn^{V}–oxo complex showed a resonance at a g value of 4.01 and displayed a six-line hyperfine splitting pattern of 113 MHz (4.04 mT, Fig. 4). A simulation using the parameters given in Table 2 reproduced the position and shape of the signal, which are indicative of a transition from the $|1^{\pm}>$ doublet of an S = 1 spin manifold. Similar to the Mn^{III}–oxo complex, the EPR signal for $[Mn^{V}H_3buea(O)]$ is sensitive only to the z component of the **g** and **A** tensors, which is aligned with the Mn^{V}–O bond. A fit to the temperature dependence of the EPR signal (Fig. S6) gave a D = +5.0(5) cm^{-1}, indicating that the $|1^{\pm}>$ doublet is 5.0 cm^{-1} above the ground |0> state.

Manganese-55 Fermi Contact Constants. The magnetic hyperfine tensor is the sum of three contributions, $\mathbf{A} = \mathbf{A}^{FC} + \mathbf{A}^{SD} + \mathbf{A}^{L}$, where A^{FC} is the Fermi isotropic contact constant, $\mathbf{A}^{SD}$ is a traceless spin-dipole tensor, and $\mathbf{A}^{L}$ is an orbital tensor. The $\mathbf{A}^{L}$ term is relatively small because the $[Mn^{n}H_3buea(O)]^{m}$ complexes have g values close to 2.00 and is ignored in our analyses. For $[Mn^{IV}H_3buea(O)]^{-}$, an $A^{FC}(^{55}Mn)$ value of −199 MHz was determined from the average of the principal components of the **A** tensor (Table 2)—this A^{FC} value is within the range found for other Mn^{IV} complexes (26, 27). Note that the sign of A^{FC} cannot be determined from EPR spectroscopy, but the values are known to be negative for manganese species (28).

For the integer-spin systems, $[Mn^{III}H_3buea(O)]^{2-}$ and $[Mn^{V}H_3buea(O)]$, only the value of A_z can be determined from the EPR spectra (Table 2). The value of $A^{FC}(^{55}Mn)$ for these two complexes was determined from the expression, $A^{FC} = A_z - A^{SD}{}_z$. The local C_3 symmetry of these complexes requires that the z component of the spin-dipolar tensor ($A^{SD}{}_z$) be coincident with

Table 2. EPR parameters for the $[Mn^nH_3buea(O)]^m$ complexes

n	S	D, cm^{-1}	E/D ($\sigma_{E/D}$)	g value	^{55}Mn A, MHz*	^{55}Mn A^{FC}, MHz	^{17}O A_z, MHz*	$\rho_\pi^\dagger$
III	2	+2.0(2)	0.055(0.030)	g_z = 2.02(1)	A_z = 280(3)	−213	7(2)	0.30
IV	3/2	+2.5(2)	0.259(0.024)	2.01(1)	165(10)‡	−199	—	—
				1.99(1)	188(2)			
				1.99(1)	244(2)			
V	1	+5.0(5)	0.005(0.003)	g_z = 1.99(1)	A_z = 113(2)	−163	10(2)	0.45

Values in parentheses are the errors associated with the measurement.
*Only the absolute value of A is determined.
†Spin population (see text for explanation).
‡A tensor rotated relative to D tensor by 36° about the *y* axis. The hyperfine pattern at g = 2.38 was not resolved, resulting in a larger uncertainty for A_x.

the Mn–O bonds. DFT calculations of $\mathbf{A}^{SD}$ have been shown to be reliable at predicting experimental $\mathbf{A}^{SD}$ tensors for other metal complexes (29). $[Mn^{III}H_3buea(O)]^{2-}$ exhibited an experimental hyperfine splitting of $A_z = \pm 280$ MHz and DFT calculations gave $A^{SD}{}_z = -67$ MHz. Because the $A^{FC}(^{55}Mn)$ value is negative, the positive possibility was discarded to give $A^{FC}(^{55}Mn) = -280 + 67 = -213$ MHz, which is in the range reported for other Mn^{III} complexes (26, 27). For $[Mn^{V}H_3buea(O)]$, an $A^{FC}(^{55}Mn)$ value of −163 MHz was determined using the same approach from the experimentally measured value for A_z (±113 MHz) and the DFT derived value for $A^{SD}{}_z$ (+50 MHz). To our knowledge, this is the first experimental report of an A^{FC} value for a Mn^V complex.

Oxygen-17 Hyperfine Constants and Spin Density. We have experimentally estimated the amount of electron delocalization within the Mn–O bond of the $[Mn^{III}H_3buea(O)]^{2-}$ and $[Mn^{V}H_3buea(O)]$ complexes, using samples that were selectively enriched with oxygen-17 (60%) at the oxido ligand. The parallel-mode EPR spectrum of $[Mn^{III}H_3buea(^{17}O)]^{2-}$ (Fig. 2, *Inset*) showed that all six hyperfine lines of the signal at g = 8.08 are broadened because of inclusion of the oxido-17 ligand (I = 5/2). This broadening was reproduced in simulations with the inclusion of a ^{17}O hyperfine constant of $A_z = 7$ (2) MHz for a 60% enrichment while keeping all other parameters unchanged from simulation of $[Mn^{III}H_3buea(^{16}O)]^{2-}$. A similar approach was used for $[Mn^{V}H_3buea(^{17}O)]$: a broadening of the hyperfine lines was found on the g = 4.01 signal in its parallel-mode EPR spectrum, which was simulated using a ^{17}O hyperfine constant of A_z = 10(2) MHz (Fig. 4, *Inset*). Related experiments with $[Mn^{IV}H_3buea(^{17}O)]^{-}$ have not yet been successful because of overlapping signals from the two doublets. Note that an Mn^{III}–(μ-O)-Mn^{IV} complex labelled with oxygen-17 showed an A-value of 13 MHz (30).

The Fermi contact value for the oxygen-17 nucleus has been expressed as $A^{FC}(^{17}O) = a_\pi\rho_\pi$, where a_π is the isotropic hyperfine constant for a spin population of $\rho_\pi = 1$ localized in a p orbital of the oxygen atom and has a value of −120 MHz for S = 1/2 (31). Similar to the ^{55}Mn hyperfine analysis, the value of $A^{FC}(^{17}O)$ was determined from $A^{FC} = A_z - A^{SD}{}_z$, where A_z is the experimentally determined value for oxygen-17 from the EPR spectra (Table 2) and $A^{SD}{}_z$ is the spin-dipolar value for oxygen-17, which is oriented along the Mn–O bond because of the local C_3 symmetry in these complexes. DFT calculations gave $A^{SD}{}_z = +37$ MHz (S = 1) for $[Mn^{V}H_3buea(O)]$. The sign ambiguity of the experimental value for A_z gave two possible values for $A^{FC}(^{17}O)$ of −27 MHz or −47 MHz, which equate to −54 MHz or −94 MHz in the S = 1/2 representation, respectively. From the above expression, these two values gave a spin population in the p orbitals on the oxido ligand of $\rho_\pi = 0.45$ or 0.78. Within the experimental uncertainty, the value of 0.45 was in agreement with the value of 0.41 determined by DFT calculations for the spin population in the p orbitals of the oxido ligand. Following a similar analysis for $[Mn^{III}H_3buea(^{17}O)]^{2-}$, DFT calculations gave $A^{SD}{}_z = +16$ MHz (S = 2). The experimentally determined value of A_z can have two possible values for $A^{FC}(^{17}O)$ of −9 MHz or −23 MHz, which equate to −36 MHz or −92 MHz in the S = 1/2 representation, respectively. Two values for the spin population in the p orbitals of the oxido ligand were obtained: $\rho_\pi = 0.30$ or 0.77, with the value of 0.30 comparing favorably to the 0.20 value determined from DFT calculations.

Discussion

Structural Properties of the Mn–oxo Complexes. The series of monomeric Mn–oxo complexes characterized in this study provide an opportunity to evaluate how the molecular and electronic structures adjust to stepwise oxidation processes. The structural results obtained from XAS experiments agreed with those predicted from DFT calculations for the optimized structures of each complex. The metrical parameters found for $[Mn^{III}H_3buea(O)]^{2-}$ from the EXAFS spectra are also in excellent agreement with those previously obtained from XRD methods. The oxidation to $[Mn^{IV}H_3buea(O)]^{-}$ produced a complex that has a strong Jahn–Teller distortion within the trigonal plane that was confirmed by EPR studies. A similar agreement between EXAFS and DFT was found for the related Mn–OH complexes, $[Mn^{III}H_3buea(OH)]^{-}$ and $[Mn^{IV}H_3buea(OH)]$ (22). There were significant changes in the metal–ligand bond lengths at the Mn center upon oxidation to $[Mn^{V}H_3buea(O)]$, with both DFT and EXAFS data showing a contraction in the Mn–O bond length to 1.68 Å. Both calculations and experiment suggest that the Mn^{III}–oxo and Mn^{V}–oxo complexes have local C_3 symmetry around the Mn centers with trigonal bipyramidal coordination geometry. The Mn^{IV}–oxo has a more distorted coordination geometry because of the Jahn Teller effect.

Correlating ^{55}Mn Hyperfine with Oxidation State. The present results indicate that the complex with the highest oxidation state

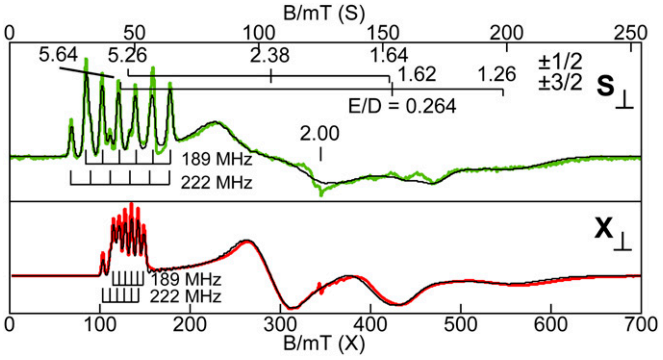

Fig. 3. S- and X-band perpendicular-mode EPR spectra of the Mn^{IV}–oxo complex, 30 mM in 1:1 DMF:THF. The black lines are simulation of the corresponding spectra using the parameters given in Table 2. Experimental conditions: temperature 12 K; frequency 3.500 GHz (S), 9.642 GHz (X); and power 0.03 mW (S), 0.20 mW (X). A minor impurity occurs near g = 2.00 in both spectra.

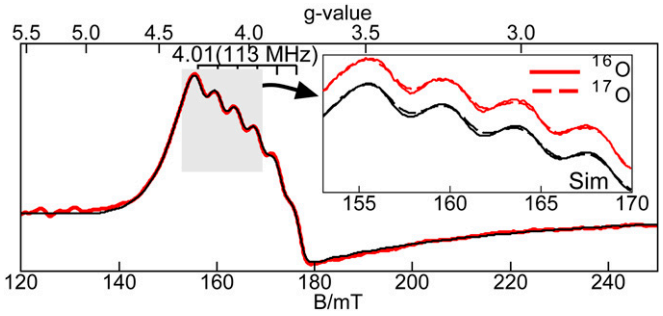

Fig. 4. X-band parallel-mode EPR spectra of the Mn^{V}–oxo complex, 25 mM in 1:1 DMF:THF. The red traces are data and the black traces are simulations. *Inset* shows the broadening of a region of hyperfine lines due to ^{17}O enrichment. Experimental conditions: temperature 11 K, frequency 9.332 GHz, and power 20 mW. The simulation parameters are given in Table 2.

within the series is an Mn^{V}–oxo species. Conceivably, the S = 1 spin state of [$Mn^{V}H_3$buea(O)] could also be produced from oxidation of the oxido ligand to an oxyl radical as opposed to a metal-centered oxidation (that is, [$Mn^{IV}H_3$buea(O•)]). For this postulated [$Mn^{IV}H_3$buea(O•)] complex, the experimentally observed S = 1 spin state would result from antiferromagnetic coupling between a Mn^{IV} center with an S = 3/2 spin state and the oxyl radical center. The observed ^{55}Mn hyperfine A values for this antiferromagnetic state would be 5/4 times greater than the intrinsic A values for the Mn^{IV} site. Our experimentally observed |A| value of 113 MHz (Table 2) therefore requires an intrinsic manganese |A| value of 90 MHz for a Mn^{IV}–oxyl complex. This |A| value is far outside the range of the A-tensor values for any known Mn^{IV} complex, including that measured for [$Mn^{IV}H_3$buea(O)]$^{-}$. Based on these experimental results, the possibility of a [$Mn^{IV}H_3$buea(O•)] species was ruled out.

The observation of EPR spectra from the [$Mn^{n}H_3$buea(O)]^{m} complexes allowed the determination of the Fermi contact term (A^{FC}) for structurally related Mn–oxo complexes (Table 2). Attempts to prepare the analogous Mn^{II}–oxo complex were unsuccessful because the oxido ligand is too basic (22), but we have previously reported the isolation of [$Mn^{II}H_3$buea(OH)]$^{2-}$, which has an experimental value of $|A^{FC}|$ = 250 MHz (32). We examined the changes in A^{FC} for this series of manganese complexes spanning four consecutive oxidation states with nearly identical molecular structures. Our findings illustrate that $A^{FC}(^{55}Mn)$ can be used to experimentally substantiate the oxidation states at the manganese centers and the covalency in the metal–ligand bonding. The value of $A^{FC}(^{55}Mn)$ depends on the polarization of the s-electron density at the nucleus, which in turn is dependent on the spin populations of the d orbitals. A correlation of $A^{FC}(^{55}Mn)$ with oxidation state and covalency was observed because the spin density of the d orbitals is affected by the extent of electron transfer from ligand to metal orbitals (that is, the amount of covalency in the M–L bonds). As the covalencies of the M–L bonds increase, the ligands donate more β-electron density to the manganese centers of the [$Mn^{n}H_3$buea(O)]^{m} complexes, leading to decreases in spin populations of the d orbitals. This decrease is detected within our EPR experiments as a reduction in the magnitude of the Fermi contact value of ^{55}Mn centers (Table 2). The experimental correlation of $^{55}Mn(A^{FC})$ values with oxidation state demonstrated that each oxidation step within the series of Mn–oxo complexes culminating in [$Mn^{V}H_3$buea(O)] is at the manganese centers and not the oxido ligands.

Spin Density Within the Mn–oxo Unit. Oxygen-17 enrichment of the oxido ligands provides a powerful probe of spin density and the presence of oxyl radicals by EPR spectroscopy. We have used this method to show that both [$Mn^{III}H_3$buea(^{17}O)]$^{2-}$ (0.30 spins) and [$Mn^{V}H_3$buea(^{17}O)] (0.45 spins) have substantial spin density on the oxido ligand, which is a consequence of strong covalent bonds within the Mn–oxo unit. The increase in spin density on the oxido ligands from [$Mn^{III}H_3$buea(^{17}O)]$^{2-}$ to [$Mn^{V}H_3$buea(^{17}O)] reveals that the covalency of the Mn–O bond increases as a function of oxidation state. The significant transfer of both α- and β-electrons into the empty Mn d_{z^2} orbital increases the electrophilicity of the oxido ligand. The spin population of the oxido ligand arising from the Mn^{V}–oxo covalency is distinct from that of an oxyl radical as illustrated by the spin densities of [$Mn^{V}H_3$buea(O)] and the corresponding Mn^{IV}–oxyl species. If [$Mn^{V}H_3$buea(O)] had been a Mn^{IV}–oxyl species, we would have observed the oxygen-17 hyperfine interaction of nearly one full spin on the oxido ligand (ρ_π close to 1) and no change in the Fermi contact value for the ^{55}Mn center between [$Mn^{IV}H_3$buea(O)]$^{-}$ and [$Mn^{V}H_3$buea(O)], both of which are inconsistent with our experimental findings (Table 2).

DFT calculations supported the Mn^{V}–oxo formulation of the ground state of [$Mn^{V}H_3$buea(O)]. Comparison of the DFT-calculated energies of the Mn^{V}–oxo complex and the higher-energy Mn^{IV}–oxyl state as a function of Mn–O bond distance (Fig. 5) clearly disfavored the Mn^{IV}–oxyl formulation; at a Mn–O bond distance of 1.68 Å corresponding to the distance determined by EXAFS measurements (Table 1), the Mn^{IV}–oxyl state is estimated to be 7,000 cm^{-1} (0.9 eV) higher in energy than the Mn^{V}–oxo ground state. The potential energy surfaces for Mn^{V}–oxo and Mn^{IV}–oxyl states cross at a Mn–O bond distance of 2.05 Å, nearly 10,000 cm^{-1} (~1.2 eV) above the ground state minimum (Fig. 5). Similar stretch-induced oxyl formation has also been observed in calculations of Fe^{IV} = O systems and stems from the propensity of a free O^{2-} ion to lower its energy by ejecting an electron (33, 34).

High-Valent Mn–oxo Site(s) Within the OEC. The premise that a Mn^{IV}–oxyl species is formed in the S_4 state of the OEC implies that an oxido ligand instead of a manganese center is oxidized in going from S_3 to S_4 to give a radical oxyl species. Computational studies of the mechanism of the OEC have suggested a Mn^{IV}–oxyl site as the key reactive species in O–O bond formation (Fig. 1*C*) (11–15). Experimental support of such a species requires systems, like the synthetic complexes considered here, that can be studied without the interference of other paramagnetic species that are present in the OEC. Our analyses of the sequential oxidation of the [$Mn^{n}H_3$buea(O)]^{m} complexes show that the manganese centers and not the oxido ligands are

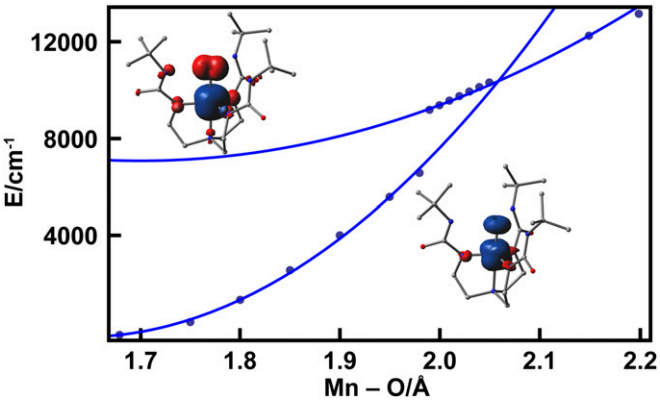

Fig. 5. Relaxed potential energy scans of the Mn^{V}–oxo (S = 1) ground state (lower curve) and the Mn^{IV}–oxyl (S = 1) broken symmetry configuration (upper curve) along the Mn–O coordinate. The solid curves are parabolic fits of the DFT-generated points obtained from B3LYP/6-311G calculations. *Insets* show total spin density contour plots for the two states.

oxidized in each species. There is neither experimental nor theoretical evidence for the formation of a Mn–oxyl radical in $[Mn^{V}H_3buea(O)]$; rather, a Mn^{V}–oxo complex is produced with an S = 1 spin ground state. The observed spin density on the oxido ligand parallels the monotonic increase in the Mn–oxo bond covalency as the oxidation state increases. A high-spin Mn^{V}–oxo site in S_4 is compatible with either mechanism outlined in Fig. 1 for the conversion of water to dioxygen within the OEC. Results from oxygen-17 labeling studies showed that the Mn–oxo unit becomes more electrophilic as the manganese center is oxidized, which would enhance its reactivity toward a nucleophile (Fig. 1*B*). Furthermore, there is appreciable spin density on the oxido ligand in $[Mn^{V}H_3buea(O)]$, suggesting that a high-spin Mn^{V}–oxo could be involved in a radical coupling process (Fig. 1*C*). For these reasons, we suggest that a high-spin Mn^{V}–oxo center should also be considered a viable candidate for the high-valent site in S_4 and possible involvement in the formation of the O–O bond.

Materials and Methods

The complexes were prepared as previously described starting from the $[Mn^{III}H_3buea(O)]^{2-}$ complex and using ferrocenium as the oxidant (19–21). Oxygen-17 samples were prepared using $H_2{}^{17}O$. The DFT calculations used the functional B3LYP and the basis set 6-311G within Gaussian 09. For details and descriptions of the experimental and computational methods and all spectral and computational data see *SI Text*.

ACKNOWLEDGMENTS. Acknowledgments are made to the National Institutes of Health (GM50781 to A.S.B. and GM77387 to M.P.H.) and the Office of Science, Basic Energy Sciences (OBES), Division of Chemical Sciences, Geosciences, and Biosciences, Department of Energy (DOE) under Contract DE-AC02-05CH11231 (to J.Y.) for financial support. Portions of this research were carried out at Stanford Synchrotron Radiation Lightsource operated by the DOE, OBES. M.P.H. recognizes National Science Foundation CHE1126268 for the purchase of the EPR spectrometer.

1. Yano J, et al. (2006) Where water is oxidized to dioxygen: Structure of the photosynthetic Mn_4Ca cluster. *Science* 314(5800):821–825.
2. Britt RD, et al. (2004) Recent pulsed EPR studies of the Photosystem II oxygen-evolving complex: Implications as to water oxidation mechanisms. *Biochim Biophys Acta Bioenerg* 1655(1–3):158–171.
3. Umena Y, Kawakami K, Shen J-R, Kamiya N (2011) Crystal structure of oxygen-evolving photosystem II at a resolution of 1.9 Å. *Nature* 473(7345):55–60.
4. Suga M, et al. (2015) Native structure of photosystem II at 1.95 Å resolution viewed by femtosecond X-ray pulses. *Nature* 517(7532):99–103.
5. Rapatskiy L, et al. (2012) Detection of the water-binding sites of the oxygen-evolving complex of Photosystem II using W-band ^{17}O electron-electron double resonance-detected NMR spectroscopy. *J Am Chem Soc* 134(40):16619–16634.
6. Pantazis DA, Ames W, Cox N, Lubitz W, Neese F (2012) Two interconvertible structures that explain the spectroscopic properties of the oxygen-evolving complex of photosystem II in the S2 state. *Angew Chem Int Ed Engl* 51(39):9935–9940.
7. Kok B, Forbush B, McGloin M (1970) Cooperation of charges in photosynthetic O2 evolution-I. A linear four step mechanism. *Photochem Photobiol* 11(6):457–475.
8. Pecoraro VL, Baldwin MJ, Caudle MT, Hsieh W-Y, Law NA (1998) A proposal for water oxidation in photosystem II. *Pure Appl Chem* 70(4):925–929.
9. Grundmeier A, Dau H (2012) Structural models of the manganese complex of photosystem II and mechanistic implications. *Biochim Biophys Acta Bioenerg* 1817(1):88–105.
10. Brudvig GW (2008) Water oxidation chemistry of photosystem II. *Philos Trans R Soc B* 363(1494):1211–1219.
11. Siegbahn PEM (2009) Structures and energetics for O2 formation in photosystem II. *Acc Chem Res* 42(12):1871–1880.
12. Cox N, Pantazis DA, Neese F, Lubitz W (2013) Biological water oxidation. *Acc Chem Res* 46(7):1588–1596.
13. Ames W, et al. (2011) Theoretical evaluation of structural models of the S2 state in the oxygen evolving complex of Photosystem II: Protonation states and magnetic interactions. *J Am Chem Soc* 133(49):19743–19757.
14. Cox N, et al. (2014) Photosynthesis. Electronic structure of the oxygen-evolving complex in photosystem II prior to O-O bond formation. *Science* 345(6198):804–808.
15. Yocum CF (2008) The calcium and chloride requirements of the O2 evolving complex. *Coord Chem Rev* 252(3+4):296–305.
16. Collins TJ, Powell RD, Slebodnick C, Uffelman ES (1990) A water-stable manganese(V)-oxo complex: Definitive assignment of a $\nu_{Mn(V)\text{-}O}$ infrared vibration. *J Am Chem Soc* 112(2):899–901.
17. Lansky DE, et al. (2005) Synthesis, characterization, and physicochemical properties of manganese(III) and manganese(V)-oxo corrolazines. *Inorg Chem* 44(13):4485–4498.
18. Groves JT, Stern MK (1988) Synthesis, characterization, and reactivity of oxomanganese (IV) porphyrin complexes. *J Am Chem Soc* 110(26):8628–8638.
19. MacBeth CE, et al. (2004) Utilization of hydrogen bonds to stabilize M-O(H) units: Synthesis and properties of monomeric iron and manganese complexes with terminal oxo and hydroxo ligands. *J Am Chem Soc* 126(8):2556–2567.
20. Parsell TH, Behan RK, Green MT, Hendrich MP, Borovik AS (2006) Preparation and properties of a monomeric $Mn^{(IV)}$-oxo complex. *J Am Chem Soc* 128(27):8728–8729.
21. Taguchi T, et al. (2012) Preparation and properties of a monomeric high-spin $Mn^{(V)}$-oxo complex. *J Am Chem Soc* 134(4):1996–1999.
22. Taguchi T, et al. (2014) Preparation and properties of an Mn^{IV}-hydroxide complex: Proton and electron transfer at a mononuclear manganese site and its relationship to the oxygen evolving complex within photosystem II. *Chem Sci* 5(8):3064–3071.
23. Weng T-C, et al. (2004) XANES evidence against a manganyl species in the S3 state of the oxygen-evolving complex. *J Am Chem Soc* 126(26):8070–8071.
24. Yano J, et al. (2007) Polarized X-ray absorption spectroscopy of single-crystal Mn(V) complexes relevant to the oxygen-evolving complex of photosystem II. *J Am Chem Soc* 129(43):12989–13000.
25. Leto DF, Jackson TA (2014) Mn K-edge X-ray absorption studies of oxo- and hydroxo-manganese(IV) complexes: Experimental and theoretical insights into pre-edge properties. *Inorg Chem* 53(12):6179–6194.
26. Stemmler TL, Sturgeon BE, Randall DW, Britt RD, Penner-Hahn JE (1997) Spectroscopic characterization of inhibitor interactions with the Mn(III)/Mn(IV) core in Lactobacillus plantarum manganese catalase. *J Am Chem Soc* 119(39):9215–9225.
27. Sinnecker S, Neese F, Noodleman L, Lubitz W (2004) Calculating the electron paramagnetic resonance parameters of exchange coupled transition metal complexes using broken symmetry density functional theory: Application to a Mn^{III}/Mn^{IV} model compound. *J Am Chem Soc* 126(8):2613–2622.
28. Freeman AJ, Watson RE (1964) *Magnetism*, eds Rado, Suhl, Vol 2A, pp 167–305.
29. Munzarova M (2004) DFT calculations of EPR hyperfine coupling tensors. *Calculation of NMR and EPR Parameters. Theory and Applications*, eds Kaupp M, Buhl M, Malkin VG (Wiley-VCH, Weinheim, Germany), pp 463–482.
30. Usov OM, et al. (2007) Hyperfine coupling to the bridged ^{17}O in the di-μ-oxo core of a Mn^{III}–Mn^{IV} model significant to the core electronic structure of the O_2-evolving complex in photosystem II. *J Am Chem Soc* 129(39):11886–11887.
31. Melamud E, Silver BL (1973) σ-π polarization parameters for oxygen-17 in organic and inorganic π radicals. *J Phys Chem* 77(15):1896–1900.
32. Gupta R, Taguchi T, Borovik AS, Hendrich MP (2013) Characterization of monomeric $Mn^{II/III/IV}$-hydroxo complexes from X- and Q-band dual mode electron paramagnetic resonance (EPR) spectroscopy. *Inorg Chem* 52(21):12568–12575.
33. Ye S, Neese F (2011) Nonheme oxo-iron(IV) intermediates form an oxyl radical upon approaching the C-H bond activation transition state. *Proc Natl Acad Sci USA* 108(4):1228–1233.
34. Srnec M, Wong SD, England J, Que L, Jr, Solomon EI (2012) π-Frontier molecular orbitals in $S = 2$ ferryl species and elucidation of their contributions to reactivity. *Proc Natl Acad Sci USA* 109(36):14326–14331.